A&A 529, A78 (2011)
DOI: 10.1051/0004-6361/201015870

Astronomy & Astrophysics

Imaging spectropolarimetry with two $LiNbO_3$ Fabry Pérot interferometers and a spectrograph

L. Kleint[1,2], A. Feller[3], and D. Gisler[1,2]

[1] Institute of Astronomy, ETH Zurich, 8093 Zurich, Switzerland
e-mail: kleintl@astro.phys.ethz.ch
[2] Istituto Ricerche Solari Locarno (IRSOL), 6605 Locarno Monti, Switzerland
[3] Max-Planck-Institut für Sonnensystemforschung, Max-Planck-Str. 2, 37191 Katlenburg-Lindau, Germany

Received 5 October 2010 / Accepted 17 February 2011

ABSTRACT

Context. Narrow-band spectropolarimetry is used to obtain information about the velocity and magnetic field structure of the solar atmosphere. Several types of instruments are suited to these observations, each with different advantages and drawbacks.
Aims. We set up a novel instrument combination using two $LiNbO_3$ Fabry Pérot interferometers (FPI), a high-resolution grating spectrograph, and the ZIMPOL system for polarimetry at IRSOL. With this system, we can carry out imaging spectropolarimetry of any spectral line from 390 to 660 nm, with a spectral resolution of 30 mÅ at 630 nm.
Methods. We describe the setup, its properties, and calculate the limitations induced by the FPI and the spectrograph. We carry out spectropolarimetric observations of the sunspot AR 11087 in different spectral lines with suitable Landé factors that could be used to derive the magnetic field strength in different height ranges of the solar atmosphere.
Results. The main advantage of our instrument compared to similar systems is that no special prefilters are required for each spectral line. A slight disadvantage is the spatial smearing induced by the dispersion of the finite transmission profiles of the FPI, which however is of the same magnitude as the seeing-limited resolution of 1–2″ at IRSOL.
Conclusions. We demonstrate that this particular instrument combination is well suited to spectropolarimetry at IRSOL.

Key words. instrumentation: interferometers – instrumentation: polarimeters – instrumentation: spectrographs – polarization – Sun: general

1. Introduction

The measurement of solar polarization with high spatial and spectral resolution provides an opportunity to investigate solar magnetic fields, the physical properties of the solar atmosphere, and the morphologic differences between the various structures on the Sun. The goal of these observations is to record a data cube with two spatial dimensions (x and y) and a spectral dimension (λ), with quasi-monochromatic wavelength points in the shortest time possible.

Several instrument principles are suitable for these observations. For example, a spectrograph can be used to get y and λ simultaneously, and by scanning across the solar surface the x dimension is recorded. This principle is used for various instruments, e.g., TIP (Mártinez Pillet et al. 1999), the DLSP (Sigwarth et al. 2001), MSDP (Mein 2002), and SOT/HINODE (Tsuneta et al. 2008). Another method is narrow-band imaging, to get x and y simultaneously, and scan through the wavelength λ using a tunable filter. Examples of these systems are Fabry-Pérot systems, which are available at many solar telescopes (e.g., Cavallini 2006; Kentischer et al. 1998; Scharmer et al. 2008). The transmission profile of Fabry-Pérot interferometers (FPI) has periodic passbands at sequential orders. For monochromatic imaging, one of these passbands has to be selected using order selectors that block the light from the remaining passbands. The most common setup is to use a narrow-band interference filter for this selection, which is straightforward to implement, but requires one prefilter for each desired spectral range. Other possibilities for order selection include using a universal birefringent filter (UBF) or a grating spectrograph.

The UBF combined with one FPI was used at the Dunn Solar Telescope (Bonaccini et al. 1989; Bonaccini & Stauffer 1990), and was capable of observing any wavelength between 4200 and 7000 Å. Seeing-limited images were possible with a high spectral resolving power of about 300 000, but the drawbacks of the system include the non-trivial tuning, because both the UBF and the FPI have periodic passbands, and the rather low transmission of the UBF (4–9%).

Setups employing a spectrograph and one-dimensional slit as an order sorter were suggested and built before (e.g., Jacquinot 1960; Wyller & Fay 1972; Cavallini et al. 1980). Cavallini et al. (1987) implemented such a setup at the Arcetri Solar Tower and obtained scientific measurements interpreting line shift and asymmetries for various solar structures. Their single observations, however, had limited spatial resolution because a photomultiplier was used. In a theoretical study, Wyller (1987) explored the possibility of obtaining 2D spectroscopic images if a field stop instead of a slit was used in combination with a FPI and spectrograph. He suggested several interesting science applications for this system, such as the possibility to simultaneously observe several parts of broad lines to derive their temperature structure or to simultaneously observe two different lines of the same atom for a differential analysis.

We implemented a setup along these lines for imaging spectropolarimetry, consisting of two Y-cut $LiNbO_3$ interferometers and a high-resolution Czerny-Turner spectrograph. We obtain simultaneous 2D images of different spectral transmission peaks on the same CCD image. Furthermore, our wavelength coverage is only limited by the coating of the FPI (3900–6600 Å), not by narrow-band interference filters, and the FPI is tunable to

any wavelength in this range. The combination with the Zurich IMaging POLarimeter (ZIMPOL) system allows polarimetry with a photon-limited accuracy of better than 10^{-4}. The system is permanently installed at the Istituto Ricerche SOlari Locarno (IRSOL), where it can be used as an alternative to the regular spectropolarimetric observations with minimal setup changes.

Because the seeing conditions at the IRSOL site are not ideal and we are in a photon starved regime because of both the comparatively small telescope aperture and the ZIMPOL instrument, our science goals differ from those of most current solar telescopes. The system allows us, for example, to study the height dependence of magnetic fields in sunspots by means of full Stokes polarization measurements. While a given spectral line has a range of formation heights that can be retrieved if inverted properly, this process is complex. It is therefore advantageous to select several different spectral lines that sample different formation height ranges in the solar atmosphere to help us with this height retrieval. Our advantage compared to other instruments is to be able to choose any desired spectral line without the need for customized prefilters. However, the spatial resolution is limited because of both the seeing and the instrument.

In this paper, we present the working principle, the advantages and disadvantages of our instrument, and a first dataset. We introduce the FPI in Sect. 2 with particular emphasis on the differences of $LiNbO_3$ interferometers compared to air-spaced interferometers. The working principle of our instrument combination is outlined in Sect. 3. The instrument setup is described in Sect. 4 and its main limitation is addressed in Sect. 5. Section 6 deals with the calibration and stability issues and a first dataset showing polarimetric images of different spectral lines is presented in Sect. 7.

2. Fabry Pérot interferometers

2.1. Summary of the theory

A FPI consists of two highly-reflecting parallel surfaces, which can be air-spaced plates or two sides of a crystal with multilayer mirror coatings on each side. Light falling on the first surface has reflected, absorbed, and transmitted components. Some of the transmitted component then passes the other surface and exits the FPI, while another part suffers inter-reflections between the two surfaces. Because of the different path lengths, a phase difference occurs and this process leads to interference and a periodically (in wavelength) repeating transmission band. The fraction of the transmitted intensity I_t relative to the incident intensity I_i can be written as (e.g., Born & Wolf 1999)

$$\frac{I_t}{I_i} = \left(1 - \frac{A}{1-R}\right)^2 \frac{1}{1 + F \sin^2 \frac{\delta}{2}}, \tag{1}$$

where A is the absorption coefficient, R the reflectivity, and $F = \frac{4R}{(1-R)^2}$. High reflectivity and low absorption are important for high throughput. The phase difference δ can be written as

$$\delta = \frac{4\pi n d \cos\theta_c}{\lambda}, \tag{2}$$

where n denotes the index of refraction, d the surface separation or the thickness of the crystal, and θ_c the angle of the beam between the reflective surfaces, which is called the inner angle. For air-spaced plates, this angle equals the incident (outer) angle θ, but in the case of a $LiNbO_3$ crystal, the inner and outer angles are significantly different and related to each other by Snell's law. The angle inside the crystal is $\theta_c = \frac{\theta}{n}$.

Two important parameters characterizing a FPI are the free spectral range (FSR) and the finesse ($\mathcal{F}$). The FSR describes the distance between two consecutive transmission maxima and depends on the wavelength. It can be increased by using several FPI in series, each with a different individual FSR. For a system with multiple interferometers, the FSR may be defined as the distance from the central transmission peak to the nearest significant transmission peak that would create overlapping images (see Sect. 3). The finesse can be written as

$$\mathcal{F} = \frac{\mathrm{FSR}}{FWHM} \approx \frac{\pi\sqrt{R}}{(1-R)}. \tag{3}$$

An ideal interferometer would have very narrow transmission peaks (i.e. minimal full width at half maximum, $FWHM$) and a large spacing between consecutive transmission maxima, thus giving a large finesse. The finesse is generally mainly influenced by the reflectivity of the surfaces which in our case is well above 90%. Surface defects can lower the effective finesse through a broadening of the transmission peaks.

2.2. Lithium niobate interferometers

2.2.1. Birefringence

We employ two FPI in series, consisting of Y-cut lithium niobate ($LiNbO_3$) with crystal thicknesses of 0.985 and 0.757 mm. The cut parallel to the optical axis introduces a birefringence, which leads to two separate passbands for two orthogonal polarization states (ordinary and extraordinary rays). The refractive indices for the two axes are $n_o = 2.3132$ and $n_{eo} = 2.2237$ for the ordinary (o) and extraordinary (eo) rays at 550 nm, and their ratio (n_o/n_{eo}) changes minimally from 1.045 to 1.037 over the wavelength range 400–1000 nm (Netterfield et al. 1997).

2.2.2. Advantages and applications of $LiNbO_3$ FPI

Most FPI systems use air-spaced interferometers where the wavelength scanning is achieved by varying the distance between the two reflecting surfaces by applying a voltage (e.g., Cavallini 2006; Kentischer et al. 1998; Scharmer et al. 2008). $LiNbO_3$ FPI have been used less (e.g., Rust 1994; Rust & O'Byrne 1991), but they offer some advantages for certain applications.

The parallelism of their reflecting surfaces is determined by their manufacture, hence the surfaces do not need to be calibrated in this respect like air-spaced interferometers. This of course implies that the manufacturing process needs to be done carefully because errors cannot be corrected later.

The different passbands of the o- and eo-rays can be used for various applications. For example, Bonaccini & Smartt (1988) suggested that small polarization signals in the solar corona can be detected by placing the o-passband on a coronal line and the eo-passband on an adjacent continuum region. The signal is then detected by subtracting the different intensities of the passbands, which are recorded by a fast switching of two orthogonal polarization states in front of the FPI. Another application was pointed out by Netterfield et al. (1997), who suggested performing a double-pass through the interferometer while rotating the polarization state by 90° between the two passes. Only the spectral region where o- and eo-passbands coincide would then be recorded, a result that is similar to that for the use of two different FPI with different plate spacings. This application was originally our reason for choosing $LiNbO_3$ over air-spaced interferometers. To our knowledge, only one other FPI made of $LiNbO_3$

is currently used for scientific measurements in the IMaX instrument of SUNRISE (Martínez Pillet et al. 2011), which however is Z-cut. Thus, rays enter parallel to the optical axis without producing different passbands for orthogonal polarization states.

2.2.3. Possibilities for tuning

$LiNbO_3$ interferometers can be tuned in three different ways: by temperature (via the temperature dependence of the index of refraction and the thermal expansion), voltage (via the electro-optic effect and the piezo effect), or tilt. The effects are described in detail in Bonaccini & Smartt (1988).

Temperature tuning is rather slow and only used to set the FPI to a "home position", for example such that at 0 V the passband is centered on the desired spectral line. It takes at least half an hour for the FPI to stabilize at the desired temperature, which can lie between 26 and 45 °C. Voltage tuning is faster and used to scan through spectral lines. The limit of 1000 V/s may not be exceeded for tuning, therefore it may take 7 s if the voltage needs to be changed from the maximum voltages of −3500 V to +3500 V. Usual scanning steps take about 0.1 s but two or three voltage jumps of 4 s duration are generally required during a scan through a spectral line.

The o-axis (X-axis of the crystal) is more sensitive to the voltage tuning by a factor of about 1.8 when compared to the eo-axis. The sensitivity increases linearly over the wavelength range and lies in the range 0.15–0.21 mÅ/V (390–650 nm) for FPI1 and 0.19–0.27 mÅ/V for FPI2. In contrast, the tuning sensitivity to temperature changes is higher for the eo-ray than for the o-ray by about a factor of two. Therefore, for our application, it is advisable to select the o-ray, which is performed through a polarizer placed in front of the first FPI.

Tilting increases the path length inside the interferometer and therefore the FPI passband is blue-shifted. The resulting wavelength shift can be written as

$$\frac{\Delta\lambda}{\lambda} \approx -\frac{1}{2}\left(\frac{\theta}{n}\right)^2 = -\frac{1}{2}\,\theta_c^2, \tag{4}$$

where the Taylor expansion for $\cos\theta_c$ is used and aborted after the first term (which is an approximation with an error of less than 1% up to a tilt angle of 45° at 5000 Å). In our case, tilting is only used for ghost elimination and not for actual tuning (see Sect. 6.1). If one FPI is tilted significantly with respect to the other, the two overlapping passbands become out of phase for points off the center of the FOV (in a collimated mount), which results in an inhomogeneous darkening across the FOV.

2.3. Different mounts

The FPI can be mounted near either a pupil plane (collimated mount) or a focal plane (telecentric mount). Both mounts have different advantages and disadvantages (e.g., Cavallini 2006).

In a collimated mount, rays from different image points pass the FPI with different angles, hence different path lengths. This implies that there is a blueshift of the transmission profile. A true monochromatic image thus needs to be constructed from several images obtained by scanning through the spectral line. This may be one of the main drawbacks of this type of mount. On the other hand, the spectral resolution is maximal, but can be degraded if the two reflecting surfaces of the FPI are not parallel. The differential blueshift ($\Delta\lambda_{\rm diff}$) if one FPI is normal to the optical axis and the other tilted by an angle θ_t can be calculated from Eq. (4) as

$$\frac{\Delta\lambda_{\rm diff}}{\lambda} \approx \frac{1}{2}\frac{\theta_t^2}{n^2} \pm \frac{\theta_t\theta_f}{n^2}, \tag{5}$$

where θ_f describes the field angle of the ray with respect to normal incidence. We define it to be positive for both directions of non-normal incidence, which results in the ± in the equation. The values for the maximum observable blueshift assuming the maximum field angle of $\theta_f = 0.37°$ in our setup are given in Table 1. For a tilt angle $\theta_t = 0.1°$, the blueshifts have a range of values. One edge of the FOV has a smaller blueshift than in the parallel case, but the opposite side of the FOV shows a significantly larger blueshift. In the collimated setup, cavity errors in the FPI can have an important influence on the image quality, but in many cases may not be significant (Righini et al. 2010).

Table 1. Blueshifts of the transmission profiles for the maximum field angles.

Tilt of FPI2	Wavelength [Å]	Max. blueshift [mÅ]	
		o-ray	eo-ray
0°	3900	15	16
0°	6600	25	28
0.1°	3900	8 . . . 24	9 . . . 26
0.1°	6600	14 . . . 41	15 . . . 45

A telecentric mount does not suffer from any blueshift. Each image point is formed by a cone of rays passing through the FPI and all image points have cones of the same angles. However, this results in a broadening of the transmission profiles and a reduction in the image quality, which are both strongly dependent on the F-number of the beam.

Weighting the advantages and disadvantages, we chose the collimated setup at IRSOL, which provides the maximum spectral resolution though not maximal spatial resolution. The spatial resolution is severely limited by seeing at the IRSOL telescope.

3. Combination of Fabry Pérot interferometers and a spectrograph

Monochromatic imaging requires us to select one of the periodically repeating FPI passbands. Figure 1 illustrates some different principles. The instrument combinations are depicted schematically on the left including the expected sample image on the camera. The panel on the right shows the different passbands for each setup, e.g. intensity versus wavelength.

Most FPI setups use a narrow-band interference filter (Fig. 1a), whose bandwidth (dotted) does not exceed the FSR of the FPI. The images are therefore quasi-monochromatic and all other transmission peaks (solid) are suppressed in the final image. The image on the camera is of maximum size or there may be two images of different polarization states for a dual beam system (not drawn).

If a grating is used with a field stop instead of a slit, all wavelengths overlap and the final image is smeared in the dispersion axis (Fig. 1b). It is therefore necessary to block unwanted wavelengths, which can be performed using a FPI (Fig. 1c). Each FPI transmission peak then results in one quasi-monochromatic image on the camera whose spatial dimension is restricted by a field stop whose size is adjusted according to the FSR of the FPI and the dispersion of the spectrograph. We note that all images are equally bright. In our case, this would result in five to eleven images, depending on the chosen FPI and the wavelength, with each sampling a different part of the spectral line.

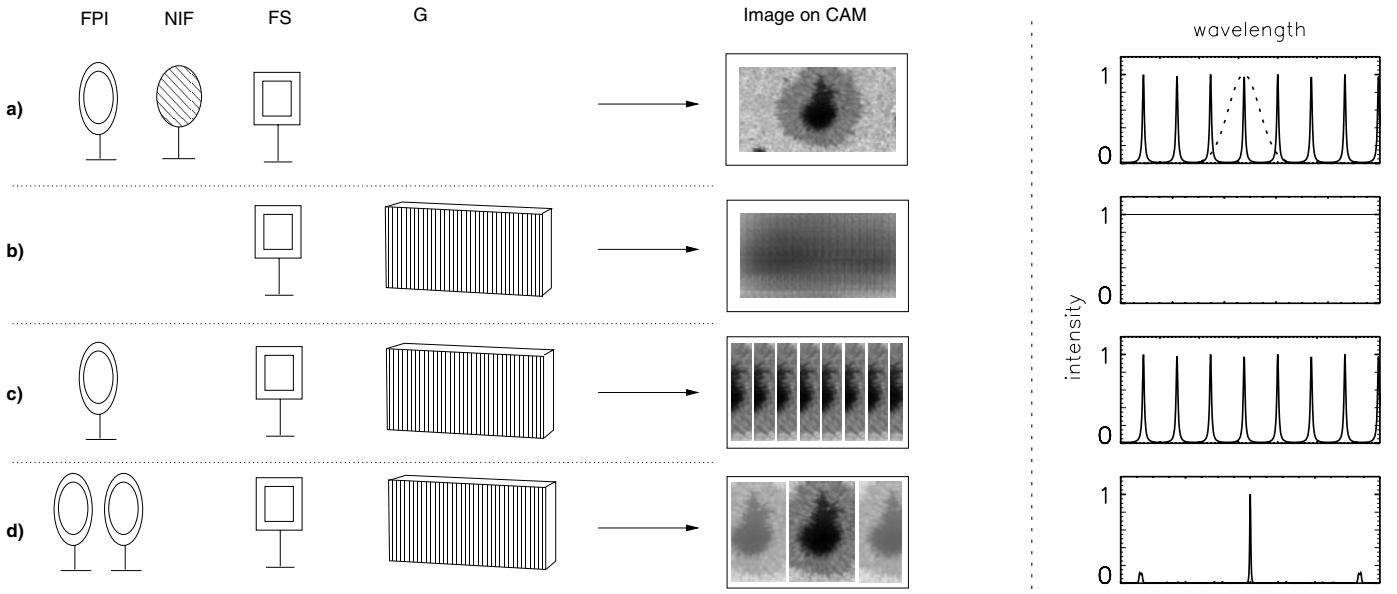

Fig. 1. Different setups (see text for explanations). *Left*: the optical components consisting of a combination of Fabry Pérot interferometers (FPI), a narrow-band interference filter (NIF), a field stop (FS), and/or a grating (G) produce different images on the camera (CAM). *Right*: the schematic passbands for each setup. The dotted curve denotes the passband of the narrow-band interference filter.

Our final setup is depicted in Fig. 1d. The combination of two FPI significantly increases the FSR, making a larger image size possible. The side transmission peaks arise from slightly overlapping passbands and their intensity is usually at least five times less than that of the main transmission peak. The magnitude and location of these side peaks can be controlled to some extent by the choice of FPI characteristics. For narrower transmission peaks, the overlaps and thus the side peaks become smaller.

4. The setup at IRSOL

In the following sections, we briefly describe the telescope and instrumentation, focusing on details that have not been published elsewhere. More details about ZIMPOL and the setup can be found in Gandorfer et al. (2004) and Kleint et al. (2008).

4.1. Telescope

The IRSOL telescope is a 0.45 m Gregory-Coudé type telescope (see Fig. 2). Light enters the evacuated tube through the entrance window and is focused onto an inclined mirror, at a distance of 2.4 m from the primary mirror, creating a solar image of size 22 mm. A pinhole of 2.7 mm allows only a small fraction of the light to pass, creating an image of 230″ diameter. The majority of the sunlight is re-imaged outside the telescope tube into an image of 7 mm diameter on a 20 mm × 20 mm chip for the purpose of guiding (Küveler et al. 1998).

The elliptical mirror, at a distance of 386 mm from the primary focus (f_1 = 386 mm) creates a focus inside the telescope building (f_2 = 4037 mm), where the spectrograph slit is usually placed. The slit is removed when the telescope is used in combination with the FPI. The effective focal length of the telescope ($f_{\rm tel}$) can be calculated using

$$\frac{1}{f_{\rm tel}} = \frac{1}{f_{\rm primary}} + \underbrace{\frac{1}{f_1} + \frac{1}{f_2}}_{1/f_{\rm ell}} - \frac{d_{\rm pe}}{f_{\rm primary} f_{\rm ell}} = 25.1\ {\rm m}, \quad (6)$$

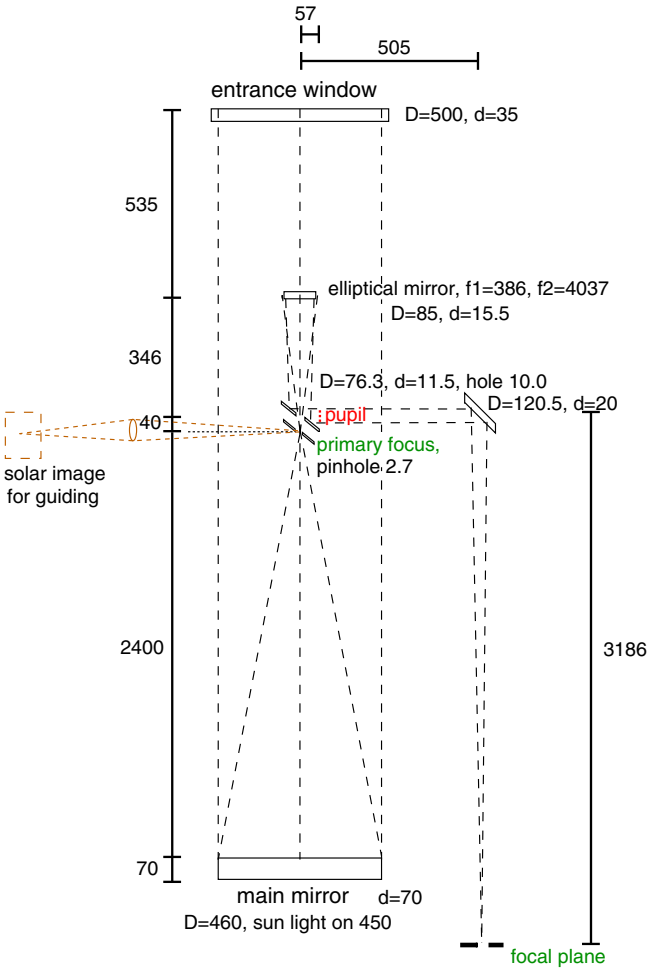

Fig. 2. Schematic drawing of the IRSOL Gregory-Coudé telescope. The distances between the optical elements are given and drawn to scale, apart from the focal length of the primary mirror (2400) and a part of f_2 of the elliptical mirror (3186) which are drawn smaller by a factor of two. All distances are given in mm.

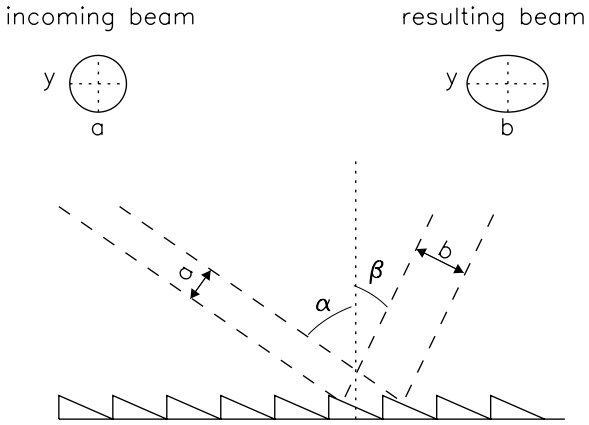

Fig. 3. Anamorphic magnification. The incoming beam is shortened/expanded in the spatial axis perpendicular to the grooves. The angles α and β are indicated with respect to the grating normal (dotted). Light rays (dashed) fall onto the grating from the left and are dispersed to the right (not to scale with IRSOL).

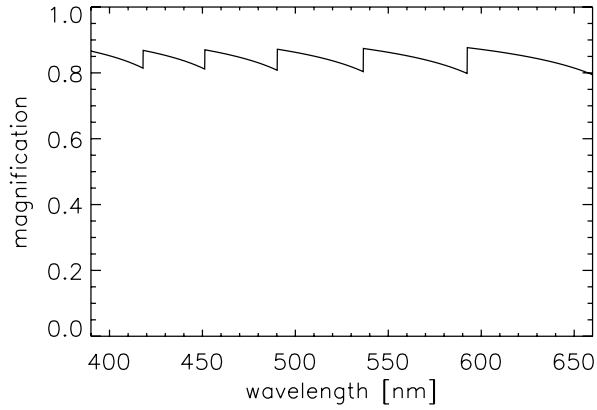

Fig. 4. Image (de-)magnification for the spectral axis calculated for the wavelength range that can be used in combination with the FPI. The discontinuities occur where the order of the spectrograph changes.

where $d_{\rm pe}$ denotes the distance between the primary and the elliptical mirror. This results in a theoretical plate scale of 8.2 arcsec/mm, which is very close to the measured value of 8.3 arcsec/mm.

4.2. The spectrograph

The Czerny-Turner spectrograph of IRSOL consists of a 180 × 360 mm (height × width) ruled grating with 316 lines/mm and a blaze angle of 63.5° in a collimated beam. The image is then projected onto the camera with an imaging mirror of 10 m focal length.

An effect to consider is the anamorphic magnification. The diameter of the beam incident on the grating is generally not preserved in the dispersion axis. Only in the Littrow-configuration or for a reflection in the zeroth order would the beam diameter remain unchanged. The effect is shown in Fig. 3. The incoming beam with axes (a, y) becomes (b, y) after the grating, according to the geometric relation

$$\frac{b}{a} = \frac{\cos\beta}{\cos\alpha}. \tag{7}$$

The figure is only schematic for a clear overview, whereas at IRSOL, incident and diffracted rays lie on the same side of the grating normal (dotted line). The grating is used in a blaze-to-collimator configuration ($\alpha > \beta$). At IRSOL, $\alpha \approx 66°$ and $\beta \approx 61°$ (at 6300 Å) and therefore the magnification amounts to 1.2, i.e. the beam is widened by 20% in the dispersion axis. This requires the camera mirror to be larger than the collimating mirror.

The second effect of the anamorphic magnification is a change in the image size on the camera. The angle dα between two rays of the same wavelength originating from different spatial points is changed on the grating according to

$$\cos\alpha \mathrm{d}\alpha + \cos\beta \mathrm{d}\beta = 0, \tag{8}$$

which can be derived from the grating equation. In our case, the angle after the grating (dβ) becomes smaller, which reduces the image size along the spectral axis ("x-direction" on the CCD) differently for each wavelength (see Fig. 4). The image demagnification is the inverse of the magnification of the beam diameter.

The theoretical spectral resolution R can be calculated using $R = mN$, where m denotes the order and N the number of grooves (316 × 360 for our case). Therefore, we expect a resolution below 1.6×10^6 for observations at 390 nm in the 14th order of the spectrograph and below 1.0×10^6 at 660 nm in the 9th order.

Custom-made, wide-band interference filters (IF in Fig. 5) with very steep cut-on and cut-off slopes act as order-sorters for the spectrograph. The wavelength range from 420 to 920 nm is fully covered through 11 filters, each with a nearly square bandpass, reaching a peak transmission from 65% (in the blue) to 85% (above 500 nm). Compared to the predisperser or formerly used filters, a factor of more than two is gained in throughput.

4.3. ZIMPOL system

The Zurich IMaging POLarimeter II (ZIMPOL) system (Gandorfer et al. 2004; Kleint et al. 2008) is used for the observations. The schematic setup of the system in combination with the spectrograph and the FPI is depicted in Fig. 5.

A Glan-Thompson polarizer and an achromatic quarter-wave plate are placed right after the exit window of the telescope. They form the calibration optics (CO), able to create any polarization state to calibrate the polarimeter. A polarization offset can cause spurious effects in the data, because calibration errors and the influence of detector nonlinearities scale with the offset. A simple solution to the problem is to introduce a polarization compensation plate (CP) made of glass, which can create any linear polarization state through a tilt and rotation about the optical axis (Thalmann 2008). When set to the opposite value of the telescope polarization, it effectively cancels the linear polarization offset up to a level of 10^{-4}. The modulator package (MP) consists of a photo-elastic modulator (PEM) with a vibration frequency of 42 kHz and an attached polarizer transforming the polarization modulation into an intensity modulation. The modulation frequency in the kHz range ensures that seeing-induced crosstalk, which may occur at modulation frequencies below several hundred Hz, can safely be neglected. With the PEM, three polarization states can be recorded simultaneously (IQV or IUV in our case). The derotator (DEROT) compensates for the image rotation induced by this type of telescope.

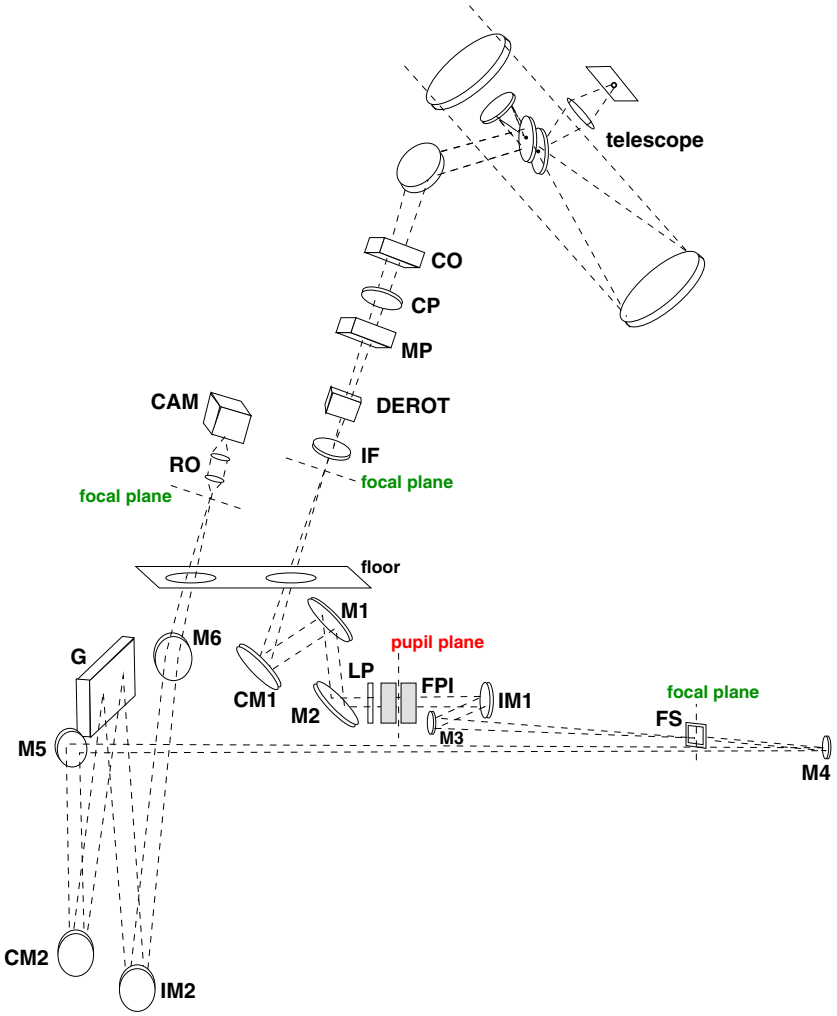

Fig. 5. Schematic drawing of the optical path at IRSOL (not to scale). See text for labels. Generally, M denotes plane mirrors, and CM and IM are mirrors with a power, either collimating or imaging the beam.

4.4. Optical setup

The setup has been optimized to allow rapid switching between the two observing modes: spectrograph only or a combination of FPI and spectrograph. For the FPI setup, only one mirror (CM1) needs to be inserted into the beam and another (not drawn in Fig. 5) removed. The additional optics in the FP setup include the elements from CM1 to M4, which create an additional focal plane. The image size and pupil positions are identical for both setups.

The beam is collimated through CM1, which is placed one focal length, 2160 mm, from the focal plane after the IF. The mirrors M1 and M2 fold the beam such that the pupil is formed between the two FPI. Both FPI are placed on an optical bench in the spectrograph room, right after a linear polarizer (LP), which selects either the o- or eo-ray. The pupil size is about 40 mm, whereas the FPI have an aperture of 60 mm. The FPI are placed on motorized sliders and can be remotely inserted into the beam. The motorized sliders were a significant improvement because any manual adjustment may introduce small tilts or shifts of the interferometers, which then require a re-calibration. After the FPI, another focal plane is created through IM1, which has the same focal length as CM1 and is placed at a distance of $2f$ from CM1 to preserve the image size and pupil positions. A field stop, or alternatively a slit for the calibrations, can be inserted here to define the image size on the camera. The distances of the folding mirrors M3 and M4 are chosen such that the focus of CM2, amounting to 9954 mm, matches the position of the field stop. The grating (G) is positioned in the collimated beam, but because of space requirements, not in a pupil plane. The mirror IM2 re-images the beam in a distance of 9955 mm, in the observing room. Exchangeable reduction optics (RO), consisting of one lens with a focal length of 296 mm and a combination of two lenses with an effective focal length of 160 mm, create an image on the camera (CAM).

Two halfwave-plates (not drawn) are additionally used in our setup. They do influence neither the optical properties nor the modulation but only serve to maximize the intensity throughput. One is placed in front of the derotator to rotate the linear polarization state such that it is parallel to the configuration of the LP. The second plate is placed after the FPI only in the o-configuration to rotate the polarization state parallel to the grooves of the grating. An improvement in the setup would be to modify the mount of the FPI, i.e. to make it rotatable around the optical axis by 90°, such that the second plate would no longer be necessary.

5. Grating-induced smearing

A drawback of this particular setup is smearing, which is caused by the dispersion of the finite-width FPI transmission profiles. If the profiles were delta-functions and therefore perfectly monochromatic, the spectrograph would disperse that wavelength to a given angle. Broader transmission profiles however consist of several wavelengths (defined by the wavelength-dependent *FWHM* $\Delta\lambda_{FWHM}$), which are dispersed in slightly

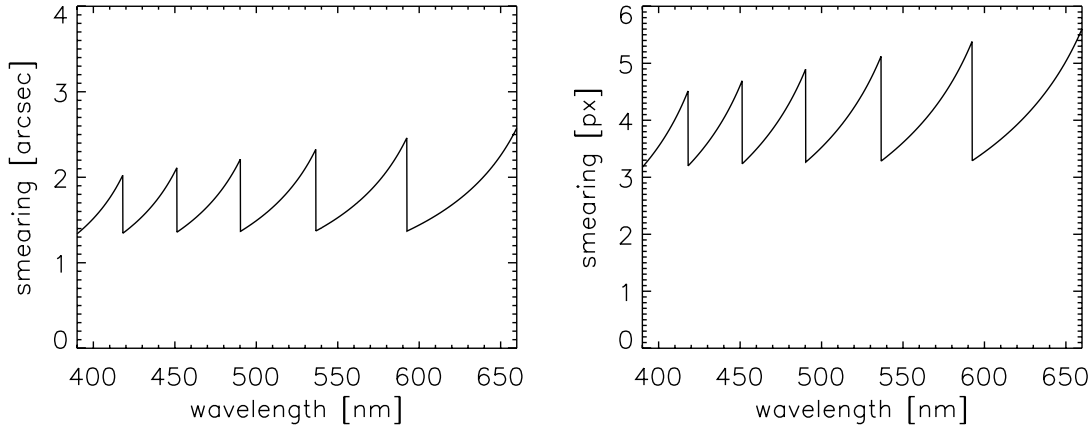

Fig. 6. Smearing in the dispersion direction of the images, induced by the finite width of the FPI transmission profiles in arcsec (*left panel*) and pixels (*right panel*).

different directions. The result is a smearing Δx in the spectral axis (x) of the image

$$\frac{\Delta x}{\Delta\lambda_{FWHM}} = \frac{m}{d_s \cos\beta} \cdot f_{\rm cam} = \frac{\sin\alpha + \sin\beta}{\lambda\cos\beta} \cdot f_{\rm cam}, \tag{9}$$

where m is the order of the spectrograph, d_s the groove spacing, and $f_{\rm cam}$ the focal length of the camera mirror. The spatial axis (y) remains unaffected. Taking into account the reduction optics factor ($r_{\rm opt}$), which reduces the effective focal length, and the pixel size ($s_{\rm px}$), the smearing in units of pixels amounts to

$$\Delta x = \frac{\sin\alpha + \sin\beta}{\lambda\cos\beta} \frac{f_{\rm cam} r_{\rm opt}}{s_{\rm px}} \Delta\lambda_{FWHM}. \tag{10}$$

Because the theoretical *FWHM* of the transmission peaks is proportional to λ^2, the smearing increases linearly with wavelength in the first order. Our observed *FWHM* is not proportional to λ^2, but closer to being linear, which we find difficult to explain. If the finesse and thus the *FWHM* were dominated by cavity errors, for example micro-roughness, this could explain the linear dependence (Feller 2007). In the following, we use the measured *FWHM* for the computations. Figure 6 shows the smearing in both pixels (right panel) and arcseconds (left panel). The conversion between the two units must take into account the anamorphic magnification, which is also wavelength-dependent, leading to a non-linear relation. Depending on the spectrograph order, $59.9° < \alpha < 72.3°$ and $55.1° < \beta < 67.5°$, which produces the oscillations and discontinuities in the figure.

The effective pixel size of the ZIMPOL camera is $22.5\,\mu\text{m} \times 90.0\,\mu\text{m}$, as given by the mask on the CCD, which reduces the resolution in the y-direction by a factor of four. In the regular spectrograph mode, this reduction is such that the image is still seeing-limited. In any imaging mode without the spectrograph, we therefore bin the image in the x-direction by four pixels. Taking into account the anamorphic magnification, binning in the FPI/spectrograph mode is wavelength-dependent and varies from 3.2 to 3.5 px.

For the current setup, the spatial smearing owing to the finite FPI bandwidth is of the order of the seeing-limited spatial resolution at IRSOL. The smearing is therefore not a critical limitation in our case, but this effect may be critical for a similar setup elsewhere, especially if a spatial resolution superior to 1″ is desired and cameras with smaller pixel sizes are used. For a given FPI (fixed *FWHM* and finesse), the optical layout may be adapted to minimize the smearing. However, this would come at the expense of reducing the overall FOV because of the different dispersion. For a given optical system, the smearing can be reduced when using FPI with a smaller *FWHM*, but if the finesse stays constant, then the FOV is reduced. A higher finesse allows a greater number of spatial points and a larger FOV for a chosen spatial resolution. Interferometers with a very high effective finesse, for example a triple FPI system such as TESOS (Kentischer et al. 1998), may be suited to high spatial resolution observations with such a system. It may be worthwhile to use air-spaced interferometers because currently, a smaller *FWHM* and a larger finesse can be achieved than with those made of $LiNbO_3$ (Gary et al. 2005).

A different solution to the problem may be achieved by a subtractive double pass, similar to the principle used by Stenflo (1973), Mein (1977), and López Ariste et al. (2010). The idea is to create a second pass of the beam through the grating where incident and diffracted angles are exchanged. The smeared image would thus disperse back to its original, un-smeared state. The side-images would need to be blocked by a field stop before the second pass through the grating to avoid light of unwanted wavelengths in the final image. The advantage is that the smearing and the anamorphic magnification can be eliminated, but the overall transmission would certainly be lowered. The final image would contain the intensities integrated over the wavelength range of one transmission peak of the FPI. Because this setup would require major changes at IRSOL and would decrease the transmission of the instrument even more, it is not implemented but should be considered for similar setups elsewhere.

6. Calibrations

We now review the calibration procedures and their stability. The FPI need to be calibrated for each desired spectral region because their voltage and temperature dependence is non-linear and cannot be modeled over the whole wavelength range. In addition, any small shift of the optics or the spectrograph renders the previous calibrations unusable. The goal of the calibration is to determine the function $V(\lambda)$, i.e. which voltage setting corresponds to a certain wavelength at a given temperature.

The wavelength scale and range first need to be determined. Therefore, a reference spectrum is taken with the FPI out of the beam. The field stop is substituted by a slit for all calibrations.

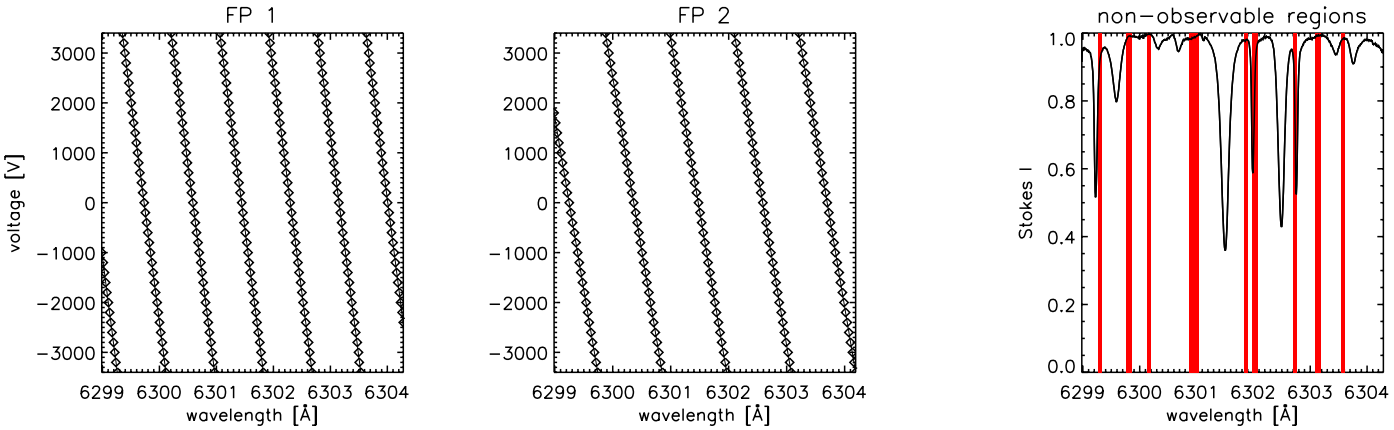

Fig. 7. Calibration functions $V(\lambda)$ for FPI1 (*left panel*) and FPI2 (*middle panel*) recorded on April 17, 2010 for the eo-axis. Linear functions (solid lines) are fitted through the measurement points (diamonds). Since the voltages cannot be tuned beyond 3500 V, there are wavelengths that cannot be set by voltage tuning in the eo-configuration (*right panel*, shaded areas).

This reference spectrum is cross-correlated with the FTS atlas (Kuruc et al. 1984).

The first FPI (FPI1) is then inserted into the beam and tilted and rotated around its axis until its surface is perpendicular to the optical axis rendering the passbands vertical on the detector and minimally wide. Once the alignment is satisfactory, a voltage scan from −3400 to +3400 V in steps of 200 V is performed. Afterwards, the same procedure is repeated with the second FPI (FPI2). The only difference is that during the alignment, FPI2 is tilted by 0.1° with respect to the optical axis to avoid inter-reflections of the interferometers on the camera image (see Sect. 6.1).

The resulting transmission spectra are fitted using an FPI transmission model to determine their position, FSR, and *FWHM*, given by

$$T = \frac{p_0}{1 + p_1 \sin^2\left(p_2(\lambda - p_4)\right)} + p_3 \tag{11}$$

with five free parameters $p_0, \ldots, p_4$ (Feller 2007). Linear fits, a good approximation within this small spectral range, are then performed to determine $V(\lambda)$. A wavelength calibration for the 6302 Å region using the eo-configuration is shown in Fig. 7. The coefficients of the linear functions are written into a ZIMPOL script and can be accessed using a function in the GUI that converts the desired wavelength into two voltages, thus centering the passbands around it.

The choice between o- and eo-ray is straightforward for our application. As mentioned in Sect. 2.2.3, the eo-ray is less sensitive to the voltage tuning. Because of the hardware limit of 3500 V for the tuning of our FPI, some wavelengths cannot be tuned in the eo-setup. This leads to gaps in the spectrum (Fig. 7, right panel), whose positions can only be shifted by temperature tuning. These gaps are more prominent at longer wavelengths where the FSR is larger. Therefore, the o-setup was used for all sunspot measurements, because there are no gaps and always at least two possible voltage settings for a given wavelength in $V(\lambda)$.

The temperature stability is very important during both wavelength calibrations and measurements and can only be achieved by placing temperature-controlled interferometers in a room with a stable ambient temperature. A FPI temperature variation of less than ±0.03 °C is usually observed during the calibration sequence. This corresponds to a wavelength variation of 4–7 mÅ over the working range of the FPI.

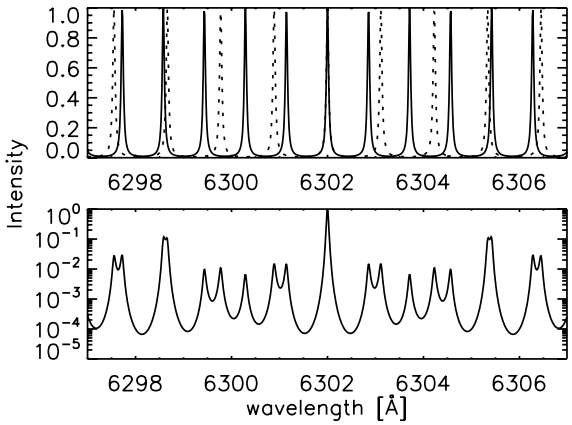

Fig. 8. *Top panel*: transmission profiles of FPI1 (solid) and FPI2 (dotted) centered at 6302 Å. *Lower panel*: resulting transmission spectrum for both interferometers. A significant ghost (11%) is located at 6302.0 ± 3.4 Å.

6.1. Ghosts

Inter-reflections between the two FPI produce ghost images. These images can be spatially separated by tilting one or both FPI. In a collimated mount, this however induces a darkening across the FOV because of a gradual detuning (Cavallini 2006). A better solution is generally to insert a prefilter between the two FPI, which is infeasible for our setup without a prefilter. Therefore, we resort to tilting FPI2 by about 0.1°, thus visibly separating the ghost images on the field stop.

Additional ghost images are caused by overlapping passbands with a finite width. Figure 8 illustrates the principle. The profiles in the top panel for FPI1 (solid) and FPI2 (dotted) are calculated using Eq. (11) with measured values of the FSR and *FWHM* for the eo-ray. In the middle of the bottom panel, we can clearly see the resulting transmission peak, and the nearby ghosts at the 1% level. At 6302.0 ± 3.4 Å, there are two peaks responsible for the two side-images as depicted in Fig. 1d. They limit the usable size of the field stop that needs to be chosen such that these ghosts do not overlap the main image. The separation and strength of the ghosts is given by the wavelength and configuration (o or eo) and influenced by both the grating position and the wavelength-dependence of the FSR and *FWHM*.

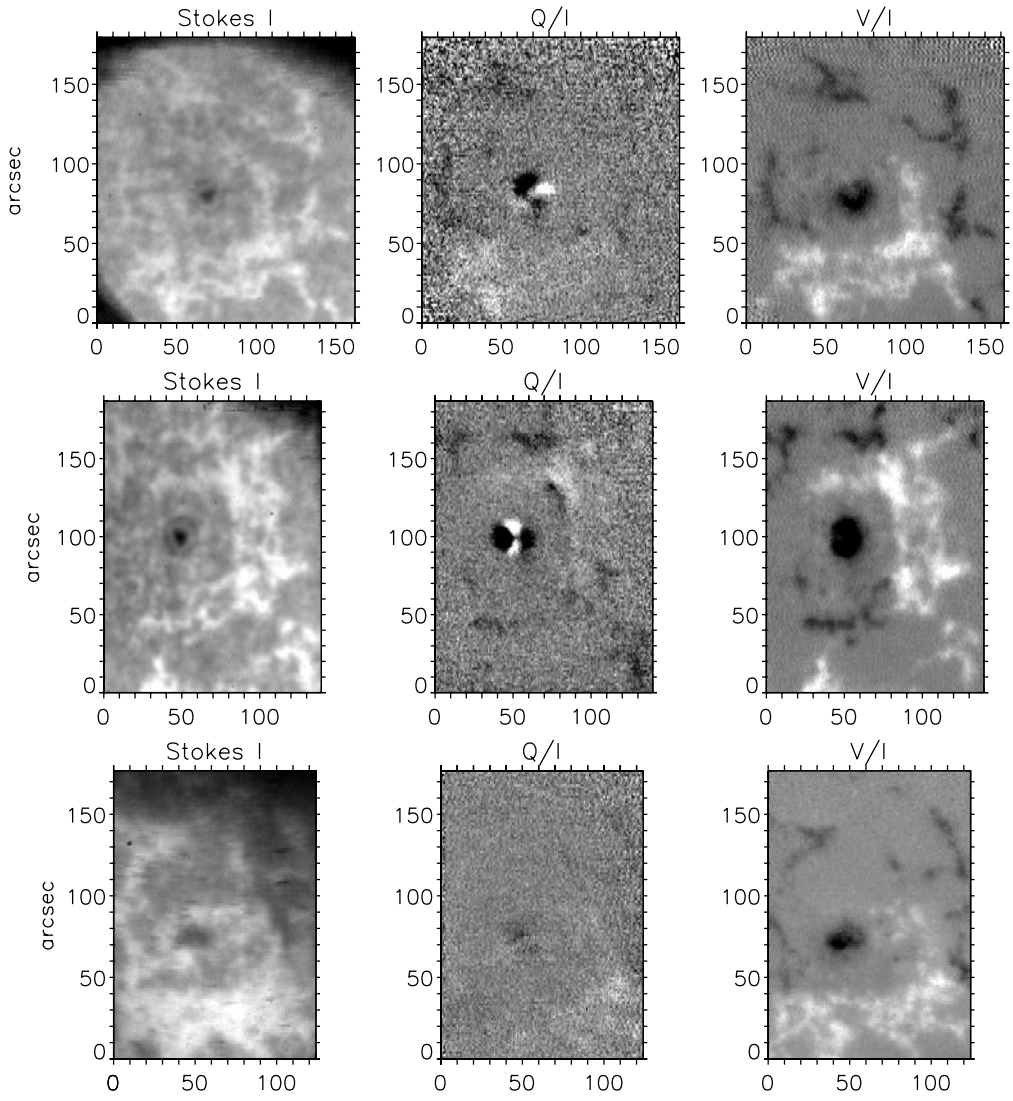

Fig. 9. Examples of line core images, Q/I and V/I (*left to right*) for the three lines Fe I 6302.5 Å, Fe I 6173.3 Å, and Na I 5895.9 Å (*top to bottom*). Greyscales: $Q/I = [-2.5, 2.5]$ % for all lines, 6302: $V/I = [-12, 13]$ %. 6173: $V/I = [-8, 8]$ %. 5896: $V/I = [-21, 16]$ %.

7. Observations

First observations of a sunspot were obtained on July 15 and 16, 2010 in the ordinary ray configuration. The target was AR 11087, a rather small sunspot close to disk center at a heliocentric angle of $\mu = 0.94$ on the first day and $\mu = 0.90$ on the second day.

Full Stokes images were taken, which requires two different positions of the PEM. Therefore, the lines were first scanned in IQV and afterwards the PEM was rotated by 45° to record IUV. Flatfields were taken for both configurations with the same wavelength steps while the telescope pointing was randomly moved around quiet Sun regions close to disk center. The flatfields are only necessary for Stokes I because the fractional polarization states ($Q/I, U/I, V/I$) are free from gain table effects. Half of the apertures of both FPI were stopped down for the observations because the transmission peaks showed an unexplained broadening when using the full aperture.

The data reduction for this particular setup is not straightforward. The image of the sunspot is located at different places on the CCD when imaging at different wavelengths. For the polarimetric calibrations, the wavelength was set to a continuum region for maximum intensity throughput. The wavelength dependence within the spectral range for one measurement (few Å) is negligible. A subframe, limited by the field stop, was selected and the modulation matrix determined for every pixel in this frame. Because the polarization calibration unit is situated before the grating, this modulation matrix can be applied to any science subframe.

For the science data, a similarly sized subframe was defined for each wavelength step. The shift of this subframe during a wavelength scan is given by the known dispersion of the spectrograph for the particular wavelength and order. The same subframes are automatically chosen for the dark images and the flatfields. Using these subframes, a standard ZIMPOL data reduction can be used (Gandorfer et al. 2004; Gisler 2005; Feller 2007).

The blueshift correction was omitted for this dataset because we only analyze the sunspot at the center of the FOV, where the value of the blueshift is similar and small for all pixels. For other applications, a blueshift map needs to be constructed from the line center positions of flatfield Stokes I profiles. This map can be used to correct for the blueshift in the data.

The sunspot was observed in four spectral regions (Fe I 6302.5 Å, Fe I 6173.3 Å, Na I 5895.9 Å, and G-band around 4310 Å) and the first three are shown in Fig. 9. Integration times were 6 s per wavelength step for the 6302 and 6173 lines and

12 s for the 5896 line for an accuracy of better than 1%. The FOV and image size are wavelength dependent, for example for the 6302 line we obtained images of size 111 px × 123 px (after binning) and a FOV of 162″ × 180″.

The images show the line core intensity (left panels) and Stokes Q/I (middle) and V/I (right). The wavelength of the shown polarization states were chosen for the maximum signal. The wavelength steps were 20 mÅ for the 6302 and 6173 lines and 25 mÅ for the 5896 line. The image orientation is the same for 6302 and 5896 but rotated by 90° for 6173, as easily visible in Stokes V/I. The image size is variable because of the ghost positions and the anamorphic magnification. The line core images of the 6302 and 6173 Å lines look very similar as both lines form in the upper photosphere. The 5896 Å line core forms higher in the solar atmosphere. We note that this image could not be flatfield-corrected because suitable flatfields were unavailable for this measurement.

Stokes Q/I images show horizontal magnetic fields occurring mainly in the penumbra. The Stokes V/I images show vertical magnetic fields in the sunspot and the surrounding network.

With suitable inversion routines, these measurements can be used to derive the magnetic field strength at different heights in the solar atmosphere. Different values have been reported for the height-dependence of the magnetic field (see Balthasar & Gömöry 2008, and references therein), usually in the range 0.5–4 G/km, and observations of many spectral lines would provide constraints on these values.

8. Conclusions

We have demonstrated that the combination of two FPI, a spectrograph, and ZIMPOL can be used for spectropolarimetric imaging of any spectral line in the range 390–660 nm. The main advantage of the instrument is that no dedicated prefilters are required for each spectral line. The main drawback is the limitation of the achievable resolution because the dispersion of the transmission profiles with a finite width causes a smearing of the image along the spectral axis (x-direction on the images). We calculated that this effect amounts to 1.5–2.5″, which is of the order of the seeing at IRSOL and acceptable for our application. For the application to larger telescopes with higher spatial resolution, the optical layout should be optimized and FPI with the smallest possible *FWHM* should be chosen to reduce the smearing. In general, this optimization will lead to a reduction in the size of the FOV. The finesse of the FPI must therefore be increased, for example with a triple-FPI system, to obtain a large FOV.

Special care needs to be taken during data reduction for this setup because in the direction of the x-axis the data are affected by anamorphic magnification, which is strongly dependent on wavelength. Therefore, to achieve the same resolution in the x and y directions on the images, a wavelength-dependent binning needs to be applied. In addition, data reduction routines need to be modified to take into account that the image is spatially shifted by several pixels on the CCD for each consecutive wavelength step. A first polarimetric dataset of a sunspot shows the expected polarization patterns and could be inverted to derive the magnetic field strength and its height-dependence.

Improvements to the current setup may include using ferroelectric liquid crystal modulators (FLC) instead of the PEM to modulate the polarization. With two FLC modulators, it is possible to obtain the full Stokes vector simultaneously. Thickness maps of the interferometers should be measured to investigate the yet unexplained broadening of the transmission profiles when using the full aperture. These maps could also be used to define suitable sub-apertures for observations.

The instrument can be used at IRSOL with minimal setup changes, and possible science applications include the investigation of the height dependence of the magnetic field, a simultaneous imaging of several parts of broad chromospheric lines to derive their temperature structure, and the simultaneous recording of the polarization of two adjacent lines to determine the filling factor of the magnetic field.

Acknowledgements. We thank Kevin Reardon for his very helpful comments on the manuscript. The technical support provided by Peter Steiner and Frieder Aebersold is gratefully acknowledged. We are grateful to Michele Bianda for his continuous support for the operation and administration of IRSOL and technical support. This work has been funded by the SNSF, grant 200020-127329. IRSOL is financed by the Canton Ticino and the city of Locarno together with the municipalities affiliated with CISL.

References

Balthasar, H., & Gömöry, P. 2008, A&A, 488, 1085
Bonaccini, D., & Smartt, R. N. 1988, Appl. Opt., 27, 5095
Bonaccini, D., & Stauffer, F. 1990, A&A, 229, 272
Bonaccini, D., Cavallini, F., Ceppatelli, G., & Righini, A. 1989, A&A, 217, 368
Born, M., & Wolf, E. 1999, Principles of Optics (Cambridge University Press)
Cavallini, F. 2006, Sol. Phys., 236, 415
Cavallini, F., Ceppatelli, G., Barletti, R., & Righini, A. 1980, A&A, 85, 255
Cavallini, F., Ceppatelli, G., Meco, M., Paloschi, S., & Righini, A. 1987, A&A, 184, 386
Feller, A. J. 2007, Ph.D. Thesis, ETH, Zurich, Switzerland
Gandorfer, A. M., Povel, H. P., Steiner, P., et al. 2004, A&A, 422, 703
Gary, G. A., Balasubramaniam, K. S., & Robinson, B. 2005, Progress Report on the Preliminary Design of a Multiple Etalon System for the Advanced Technology Solar Telescope
Gisler, D. 2005, Ph.D. Thesis, ETH, Zurich, Switzerland
Jacquinot, P. 1960, Reports on Progress in Physics, 23, 267
Kentischer, T. J., Schmidt, W., Sigwarth, M., & Uexkuell, M. V. 1998, A&A, 340, 569
Kleint, L., Feller, A., & Bianda, M. 2008, in Ground-based and Airborne Instrumentation for Astronomy II, ed. I. McLean, & M. Casali, Proc. SPIE, 7014, 701414
Kurucz, R. L., Furenlid, I., Brault, J., & Testerman, L. 1984, Solar flux atlas from 296 to 1300 nm (Sunspot, NM)
Küveler, G., Wiehr, E., Thomas, D., et al. 1998, Sol. Phys., 182, 247
López Ariste, A., Le Men, C., Gelly, B., & Asensio Ramos, A. 2010, Astron. Nachr., 331, 658
Mártinez Pillet, V., Collados, M., Sánchez Almeida, J., et al. 1999, in High Resolution Solar Physics: Theory, Observations, and Techniques, ed. T. Rimmele, K. S. Balasubramaniam, & R. Radick, ASP Conf. Ser., 183, 264
Martínez Pillet, V., Del Toro Iniesta, J. C., Álvarez-Herrero, A., et al. 2011, Sol. Phys., 268, 57
Mein, P. 1977, Sol. Phys., 54, 45
Mein, P. 2002, A&A, 381, 271
Netterfield, R. P., Freund, C. H., Seckold, J. A., & Walsh, C. J. 1997, Appl. Opt., 36, 4556
Righini, A., Cavallini, F., & Reardon, K. P. 2010, A&A, 515, A85
Rust, D. M. 1994, Optical Engineering, 33, 3342
Rust, D. M., & O'Byrne, J. W. 1991, in Solar Polarimetry, ed. L. J. November, 74
Scharmer, G. B., Narayan, G., Hillberg, T., et al. 2008, ApJ, 689, L69
Sigwarth, M., Berst, C., Gregory, S., et al. 2001, in Advanced Solar Polarimetry – Theory, Observation, and Instrumentation, ed. M. Sigwarth, ASP Conf. Ser., 236, 57
Stenflo, J. O. 1973, Appl. Opt., 12, 805
Thalmann, C. 2008, Ph.D. Thesis, ETH, Zurich, Switzerland
Tsuneta, S., Ichimoto, K., Katsukawa, Y., et al. 2008, Sol. Phys., 249, 167
Wyller, A. A. 1987, in The Role of Fine-Scale Magnetic Fields on the Structure of the Solar Atmosphere, ed. E.-H. Schröter, M. Vázquez, & A. Wyller, 335
Wyller, A. A., & Fay, T. 1972, Appl. Opt., 11, 1152